Estimation of flow direction in meandering compound channels

Xingnian Liu [1], Qin Zhou [1], Sheng Huang [1], Yakun Guo [2], Chao Liu [1*]

1. State Key Laboratory of Hydraulics and Mountain River Engineering, Sichuan University, Chengdu 610065, China
2. School of Engineering, University of Bradford, BD7 1DP, UK

[*]**Corresponding author**: Chao Liu, Email: liuchaoscu@vip.qq.com

Liu X. N (liuxingnian@126.com); Zhou Q. (55204093@qq.com); Huang S. (690929318@qq.com); Guo Y. K. (Y.Guo16@bradford.ac.uk); Liu C. (liuchaoscu@vip.qq.com)

Highlights:

(1) The depth-averaged two-dimensional flow direction between the entrance and apex sections is predicted.

(2) The vertical profile of local flow angles is linked to the secondary current cell.

(3) The means of the local flow angles within and above the secondary current cell are separately discussed.

(4) The proposed model is verified using published data from five sources.

Abstract: The flow in the main channel of a meandering compound channel does not occur in the ridge direction because of the effect of the upstream floodplain flows. This study proposes a model for estimating the flow direction in the depth-averaged two-dimensional domain (depth-averaged flow angles) between the entrance and the apex sections. Detailed velocity measurements were performed in the region between the meander entrance section and apex section in a large-scale meandering compound channel. The vertical size of the secondary current cell is highly related to the depth-averaged flow angle; thus, the means of the local flow angles above the secondary current cell and within the cell are separately discussed. The experimental measurements indicate that the mean local flow angle above the cell is equal to the section angle, whereas the mean local flow angle within the cell is equal to zero. The proposed model is validated using published data from five sources. Good agreement is obtained between the predictions and measurements, indicating that the proposed model can accurately estimate the depth-averaged flow direction in the meandering compound channels. Finally, the limitations and application ranges of the model are discussed.

Keywords: depth-averaged two-dimensional flow direction, depth-averaged flow angle, secondary current cell, meandering compound channel, overbank flows

1. Introduction

Natural rivers form meanders due to the sediment transport and bed erosion. Throughout the year, the water in a meandering channel (i.e., the inbank flow) typically flows downstream in the ridge direction. However, when river flood occurs, the floodplains on the two sides of the main river are inundated, forming a meandering compound channel in which the floodplain water and main channel water have different depth-averaged two-dimensional flow directions in the meandering belt, particularly within crossover sections (Shiono et al. 2009; Liu et al. 2014). Numerous previous studies have investigated the complex three-dimensional flow patterns along meanders in meandering channels with overbank flows (e.g., Shiono and Muto 1998; Lyness et al. 2001; Spooner 2001; Wormleaton et al. 2004; Shiono et al. 2008, 2009; Liu et al. 2016a) and found that the upstream floodplain flow can significantly affect the main channel flow in crossover sections. For example, the mean velocity in a meandering main channel reaches a maximum at the apex section and a minimum in crossover sections because of the influence of upstream floodplain flows (Liu et al. 2014, 2016a). Floodplain roughness (e.g., vegetation) is an important factor that affects the flow pattern along a meander (Shan et al. 2017). For example, under low-flow conditions, roughened floodplains enhance the conveyance capability of the main channel but reduce the conveyance capability of the entire channel (Shiono et al. 2009; Liu et al. 2016a). These studies provide insights to better understand the evolution of the flow along a meander.

A secondary current cell is a typical flow feature found in a meandering main channel and has been extensively investigated (Sellin et al. 1993; Shiono and Muto 1998; Wormleaton et al. 2004; Liu et al. 2014, 2016a; Shan et al. 2017). In half of a meander (from one apex section to the next apex section), a secondary current cell initially appears next to the inner corner in the section after the apex section. The cell expands in both the lateral and vertical directions as the section proceeds. The maximum size of the secondary current cell is eventually observed at the next apex section. The cell then rapidly decays after the apex section and disappears before the formation of a new cell (see Fig. 8b in Liu et al. 2016a). A similar development process of secondary current cells was reported based on experimental observations (e.g., Shiono et al. 2008) and numerical simulations (e.g., Jing et al. 2009). In this study, we focus on the flow direction in the depth-averaged two-dimensional region between the entrance section and apex section (e.g., the region between CS5 and CS7 in Fig. 1), where secondary current cells are approximately fully developed. At the meander entrance (CS5), the cell fills the region below the bankfull level because of the suppression effect from upstream floodplain flow. As the section proceeds (i.e., a smaller section angle, θ_x, is formed, as defined in Fig. 1), the effect of upstream floodplain flow on the secondary current cell gradually decreases; thus, the cell further expands in the vertical direction. The secondary current cell occupies the entire main channel in the apex section (CS7) because of the negligible effect of the floodplain flow (see Liu et al. 2014).

The generation mechanisms of secondary flows indicate that the intensities of secondary flows in the meandering main channel are

significantly enhanced compared to those in a straight channel due to the contributions of centrifugal forces (Liu et al. 2013, 2014, 2016a). For overbank flows, considering the influence of upstream floodplain flows, the water in the main channel in the region between an entrance section and apex section does not flow downstream in the ridge direction, except in apex sections (e.g., see Fig. 9 in Liu et al. 2014). The depth-averaged two-dimensional flow direction θ_a ($= \frac{1}{H}\int_0^H \theta(z)\,dz$) is defined to quantitatively express this phenomenon, where *H* is the flow depth and $\theta(z)$ is the local flow angle ($= arctan\frac{V}{U}$, in which *U* and *V* are time-averaged velocities in the streamwise and lateral directions, respectively, and *z* is the vertical position). Previous studies have discussed the planform of θ_a in different situations. The relative flow depth *Dr* (= (*H*-*h*)/*H* with bankfull level *h*) is often used in compound channels. For example, Shiono and Muto (1998) reported that in cases with the same *Dr* (= 0.5), $\theta_a = 26.5°$ to $30°$ in the entrance section ($\theta_x = 60°$), $\theta_a = 17°$ to $19.4°$ in the middle section ($\theta_x = 30°$), and $\theta_a = -9°$ to $-2°$ in the apex section ($\theta_x = 0°$). Their observations indicate that θ_a reaches a maximum in the entrance section because the entrance section has the largest θ_x ($= 60°$). In contrast, θ_a is close to $0°$ in the apex section because the apex section has the smallest θ_x ($= 0°$). Thus, θ_a is associated with the position of the section (i.e., section angle θ_x). In this study, as we focus on the region between the entrance section and apex section, θ_x ranges between $0°$ and the geometrical angle of the region θ_{geo} (i.e., $\theta_{geo} \geq \theta_x \geq 0°$). Therefore, θ_{geo} can affect the value of θ_x and the value of θ_a. However, θ_{geo} is initially determined when the curve of the meandering main channel is

prescribed. Furthermore, in a given section (i.e., for a given θ_x), θ_a varies with *Dr*. For example, in the entrance section ($\theta_x = 60°$), Shiono and Muto (1998) reported that $\theta_a = 1° \; to \; 5°$ (close to 0°) when *Dr* = 0 (the inbank flow), indicating that the water flows downstream in the ridge direction. This behavior occurs because no upstream floodplain flow affects the main channel flow. In contrast, under high-flow conditions, the upstream floodplain flow plunges into the main channel and affects the secondary flows and the flow direction. For example, Liu et al. (2014) found that $\theta_a = 26° \; to \; 32°$ at *Dr* = 0.45 in the entrance section ($\theta_x = 60°$). Overall, previous studies have suggested that θ_a is related to three factors, namely θ_x, θ_{geo} and *Dr*.

Several depth-averaged two-dimensional numerical models have been used to determine the planform of the depth-averaged velocity, including the velocity orientation and magnitude (e.g., Chen et al. 2015; Harison et al. 2015; Ding et al. 2017). However, the modeling results of flow direction (orientation) cannot be validated using measured data under high flows because flow measurements during heavy flooding periods are not available. Therefore, a method for estimating the depth-averaged two-dimensional flow direction in a meandering main channel with overbank flows is required. To this end, the goals of this study are to (1) conduct laboratory experiments and measurements in the region between the entrance section and apex section in a meandering compound channel; (2) understand how the vertical profiles of local flow angles are related to secondary current cells; (3) propose a method to estimate the depth-averaged two-dimensional flow direction (i.e., depth-averaged

flow angle); and (4) validate the proposed model using published experimental data from five sources and (5) discuss the applications and limitations of the model.

2. Experimental Methods

The experiments were performed in a 35-m-long, 4-m-wide and 1-m-high meandering compound channel at Sichuan University. The total discharge (Q) in the meandering compound channel was measured by a triangular weir that was installed in front of the flume. The sinuosity of the main channel (s) was defined as the ratio of the wavelength (L_w) to the valley length (L_v) in half of a meander, i.e., $s = L_w/L_v$ (see Fig. 1). The same definition of sinuosity was used as reported in five previous studies (see Section 4), which are used for validation. In this study, s = 1.381. The valley slope (S) was 1‰, and thus, the slope of the meandering main channel was 0.7‰ (= S/s). The width (b) and depth (h) of the meandering main channel were 0.7 m and 0.14 m, respectively, yielding b/h = 5. The inner radius (r) was 0.9 m. The geometrical angle, θ_{geo}, of the region between the entrance section (CS5) and apex section (CS7) was 60°. The channel bed and vertical walls on the two sides of the main channel and on the two sides of the floodplains were smoothened using concrete, producing a Manning's roughness parameter of n = 0.015. The flow depth in the main channel (H) was 25.5, 21.6 and 18.9 cm in cases MN1, MN2 and MN3, respectively. The height of the secondary current

cell (h_0) varied in the region between the entrance section and apex section at different flow depths (see Table 1). The flow in the channel was fully developed, with a Reynolds number of *Re* = 19,000 to 42,000 based on $Re = \frac{QR}{Av}$, where *A* is the cross-sectional area in an apex section, *R* is the hydraulic radius of the apex section, and *v* is the kinematic viscosity (= 10^{-6} m^2/s). The tailgate was modified to ensure that the water surface slope was parallel to the valley slope to establish quasi-uniform flow conditions. The experimental parameters are listed in Table 1.

In this study, we propose an estimator for the depth-averaged flow angle between the entrance section (CS5) and the apex section (CS7). Thus, velocity measurements were performed at CS5, CS6 and CS7. In each section, measurements were performed at 13 measurement lines in the meandering main channel (see Liu et al. 2014 and 2016a) at three relative flow depths (*Dr* = 0.25, 0.35 and 0.45). The lateral positions of the measurement lines in the main channel were *y* = 5, 10, 15, 20, 25, 30, 35, 40, 45, 50, 55, 60 and 65 cm. The intervals of the two vertical points were identical (1.5 cm) in the three cases. A Sontek Acousitc Doppler Velocimeter (ADV) with upside and downside probes was used to record velocity data at each point, with a sample recording frequency of 50 Hz and a duration of 30 s. The raw velocity data were processed using the despiking method of Goring and Nikora (2002). The processed data were then used to decompose the time-averaged velocity (*U*, *V* and *W*). Thus, the local flow angle $\theta(z)(= arctan\frac{V}{U})$ in the main channel and the depth-averaged flow angle (θ_a) could be obtained. The lateral mean of θ_a in a specific section in the meandering main channel can be expressed as $\theta_{a(m)} = \sum_1^N \theta_a$, where *N* is the number of measurement lines (e.g., *N* =

13 in this study, see Fig. 1b). In addition, it is expected that the conveyance capability of the meandering main channel is related to the depth-averaged flow angle; thus, the relation between the main channel discharge (Q_{mc}) and the mean depth-averaged flow angle ($\theta_{a(m)}$) will be discussed, where Q_{mc} was obtained by integrating the measured velocities over the main channel.

3. Theoretical Consideration

The secondary current cell fully develops below the bankfull level at the entrance section (CS5) of a meander bend. A secondary current cell occupies the region below the bankfull level of the main channel (z = 0 to h) at CS5, as denoted by the blue circle with arrows in Fig. 2a. Then, the cell continues to expand in the vertical direction at CS6 (Fig. 2b). This trend occurs because a small θ_x $(= 30°)$ at CS6 leads to a small suppression effect of upstream floodplain flows on the secondary current cell compared to that at CS5 ($\theta_x = 60°$). Finally, the secondary current cell occupies the entire main channel in the apex section (CS7) (Fig. 2c) due to the negligible effects of upstream floodplain flows (see the discussion in Liu et al. 2014). In addition, Fig. 2 illustrates that the distance between the cell bottom (z = 0 cm) and center ($z = h_{0(c)}$) is the same as the distance between the cell top ($z = h_0$) and center ($z = h_{0(c)}$), such that $h_{0(c)} = h_0/2$ within a range of uncertainty (see the numbers in Table 1). The height of the cell (h_0) and the distance between the cell bottom and center ($h_{0(c)}$) vary as the section proceeds. Notably, h_0 is related

to the position of the section (θ_x) between the entrance and apex sections, as well as the flow depth (H). Specifically, $h_0 \approx h$ at the entrance of the meander bend (CS5, $\theta_x = 60°$), $h_0 = H - 0.5(H - h)$ in the middle section (CS6, $\theta_x = 30°$) and $h_0 \approx H$ in the apex section (CS7, $\theta_x = 0°$). In the same section (e.g., apex section CS7), H (i.e., Dr) determines h_0. For example, at CS7, $h_0 \approx 24.5 \pm 1.5$ cm at $Dr = 0.45$, but $h_0 \approx 17.5 \pm 1.5$ cm at $Dr = 0.26$ (see Table 1). Thus, h_0 can be predicted using $h_0 = H - k(H - h)$, where $k = \frac{\theta_x}{\theta_{geo}}$. Here, $\theta_x = 60°$ ($k = 1$) and $\theta_x = 0°$ ($k = 0$) represent the entrance section and the apex section, respectively (see Fig. 1a). The predicted value of h_0 is equal to the measured h_0 within a range of uncertainty (Fig. 3). However, h_0 should be related to the curve of the meandering main channel. In this study, we use a one-third circle line to reflect this curve (with angle $120°$ in the meander bend, see Fig. 1a).

The depth-averaged flow angle, θ_a, is calculated as follows:

$$\theta_a = \frac{1}{H}\left(\int_0^{h_0} \theta\,(z)dz + \int_{h_0}^{H} \theta\,(z)dz\right) \quad (1)$$

Rearranging Eq. (1) yields:

$$\theta_a = \frac{h_0}{H}\left(\frac{1}{h_0}\int_0^{h_0} \theta\,(z)dz\right) + \frac{H-h_0}{H}\left(\frac{1}{H-h_0}\int_{h_0}^{H} \theta\,(z)dz\right) \quad (2)$$

Based on the generation mechanism of secondary flows in the meandering main channel, secondary flows consist of enhanced original

secondary flows and the components of upstream floodplain flows (Liu et al. 2014). Considering the vertical size of the secondary current cell (see Fig. 2), the local flow angle averaged over the height of the cell (θ_{cell}) and mean local flow angle above the cell (θ_{upper}) must be considered separately. These variables can be expressed as follows:

$$\theta_{cell} = \frac{1}{h_0}\int_0^{h_0} \theta\,(z)dz;\ \theta_{upper} = \frac{1}{H-h_0}\int_{h_0}^{H} \theta\,(z)dz \quad (3)$$

Thus, Eq. (2) can be rewritten as:

$$\theta_a = \frac{h_0}{H}\theta_{cell} + \frac{H-h_0}{H}\theta_{upper} \quad (4)$$

In addition, $h_0 = H - k(H-h)$ can be rearranged to $\frac{h_0}{H} = 1 - kDr$ and $\frac{H-h_0}{H} = kDr$. Thus, Eq. (4) can be rewritten as follows:

$$\theta_a = (1-kDr)\theta_{cell} + kDr\theta_{upper} \quad (5)$$

To solve Eq. (5), θ_{cell} and θ_{upper}, which depend on the vertical distribution of $\theta(z)$ in different sections, must be separately discussed. The vertical profiles of $\theta(z)$ at the centerline of the secondary current cell for MN1 at CS5 (entrance section), CS6 (middle section) and CS7 (apex section) are shown in Fig. 4. First, in the region of the secondary current cell (z = 0 to h_0), the vertical integration of $\theta(z)$ between z = 0 and h_0 (i.e., θ_{cell}) is approximately equal to $0°$ from CS5 to CS7. Specifically, at Dr = 0.45, $\theta_{cell} = -0.3 \pm 2.6°$ from CS5 to CS7 (red lines in Fig. 4). Similarly, $\theta_{cell} = -0.3 \pm 2.3°$ at Dr = 0.35 and $\theta_{cell} = 0.3 \pm 2.7°$ at Dr = 0.25 (see Table 3). Second, at the crossover section

where $\theta_x > 0$ (e.g., CS5 and CS6), $\theta_{upper} \approx \theta_x$ above the cell. Specifically, $\theta_{upper}/\theta_x = 1.0$ to 1.1 (green lines in Figs. 4a and 4b). Similarly, $\theta_{upper}/\theta_x = 1.0$ to 1.2 at *Dr* = 0.35 and 1.0 to 1.3 at *Dr* = 0.25 (see Table 3). Therefore, two relations can be obtained:

$$\theta_{cell} = 0° \quad (6a)$$

$$\theta_{upper} = \theta_x \quad (6b)$$

The sizes of the secondary currents at CS5, CS6 and CS7 are different, indicating that Eq. (6a) is independent of the size of the secondary current cell.

Next, the mean value of θ_{cell} in the lateral direction (i.e., $\theta_{cell(m)} = \frac{1}{b}\int_0^b \theta_{cell}\, dy$) can be calculated, and the mean value of θ_{upper} in the lateral direction (i.e., $\theta_{upper(m)} = \frac{1}{b}\int_0^b \theta_{upper}\, dy$) is compared to θ_x. Based on the data from MN1 to MN3, $\theta_{cell(m)} = 1.7 \pm 3.8°$ and $\theta_{upper(m)}/\theta_x = 1.0 \pm 0.1$. Thus, $\theta_{cell(m)} = 0°$ and $\theta_{upper(m)} = \theta_x$. In addition, the local flow angle at the center of the secondary current cell should be zero because the velocities in the lateral and vertical directions (*V* and *W*) are approximately zero (see Fig. 2). Thus, the value of $h_{0(c)}$ can be determined by the vertical distribution of $\theta(z)$ at the centerline of the secondary current cell. Specifically, $h_{0(c)}$ is the distance from the channel bed to the position at which $\theta(z) \approx 0°$ in the *z*-direction (see Fig. 4).

Although Eq. (4) can be simplified as $\theta_a = \frac{H-h_0}{H}\theta_{upper}$ using Eq. (6a), θ_a is related to the height of the secondary current cell (h_0), flow

depth (H) and θ_{upper}. Thus, the size of the secondary current cell (e.g., h_0) can affect θ_a. For example, $h_0 \approx h$ at CS5, and the upstream floodplain flow exceeds the bankfull level (h) and influences θ_a. However, at CS7, $h_0 \approx H$ indicates that secondary currents occupy the entire main channel; therefore, these currents determine θ_a. Overall, h_0 represents the effect of secondary currents on the depth-averaged flow angle (θ_a). In addition, it is worth further discussing the relation between θ_a and H (i.e., Dr). When inbank flow occurs, $h_0 \approx H$, yielding $\theta_a = \theta_{cell} = 0°$ because no upstream floodplain flow affects the depth-averaged two-dimensional flow direction. When overbank flow occurs, at the same section (the same h_0), a large H leads to a large proportion of θ_{upper} in Eq. (4), representing the considerable influence of the upstream floodplain flow on the depth-averaged flow angle (θ_a).

Eq. (5) can be combined with Eq. (6a and 6b) and rearranged in the range of $H \geq h_0 \geq h$, corresponding to $\theta_{geo} \geq \theta_x \geq 0°$ (i.e., $1 \geq k(= \frac{\theta_x}{\theta_{geo}}) \geq 0$).

$$\theta_a = kDr\theta_x = Dr\frac{{\theta_x}^2}{\theta_{geo}} \quad (7)$$

Eq. (7) can be further simplified in the entrance section (CS5) and apex section (CS7). Specifically, $\theta_a = Dr\theta_{geo}$ at CS5 ($h_0 = h$, i.e., $\theta_x = \theta_{geo}$), and $\theta_a = 0°$ at CS7 ($h_0 = H$, i.e., $\theta_x = 0°$). In the apex section, water in both the main channel and floodplain flows downstream

in the same direction (valley direction); thus, the main channel flow is not affected by upstream floodplain flow (i.e., $\theta_a = 0°$ at CS7). The mean depth-averaged flow angle in a section, $\theta_{a(m)}$ $(= \frac{1}{b}\int_0^b \theta_a \, dy)$, is equal to θ_a because θ_x remains the same in the lateral direction (y-direction) in each section. However, this model was proposed for meandering channels with overbank flow. For a channel with inbank flow, particularly in a sharply curved bend with a mobile bed, in which secondary current cells are not well developed in the lateral direction (e.g., Blanckaert 2010), this model may be unable to accurately predict θ_a. This potential model limitation will be discussed later in this paper.

4. Published Data

The experimental data presented in five previously published studies are used to verify the proposed model. Shiono and Muto (1998), Muto (1997), Patra et al. (2012) and Shiono et al. (2009) described the details of the laboratory flume experiments. Harrison et al. (2015) described the numerical simulation of field observations in the Merced River, California. The data between the entrance section and apex section from above five studies are used for validating the proposed model. Though the details of the experiments and numerical simulation can be found in Shiono and Muto (1998), Muto (1997), Patra et al. (2012) and Shiono et al. (2009) and Harrison et al. (2015); a brief description of the experiments and numerical simulation is presented for completeness and convenience. The symbols for each case in Tables 1 and 2 are the same

in the following text and figures.

(1) The experiments of Shiono and Muto (1998) and Muto (1997) were conducted in the same flume, in which two channels with different main channel sinuosities were considered. These two experiments were conducted in a 10.8-m-long, 1.2-m-wide and 0.33-m-high meandering compound channel with a valley slope (S) of 1‰. Quasi-uniform flow was achieved by controlling the tailgate. The geometrical angle, θ_{geo}, of the region between the entrance section and apex section was $60°$. The main channel width (b) and depth (h) were 15 cm and 5 cm, respectively, producing b/h = 3. The positions of the vertical measurement lines in the main channel were y = 0.5, 1, 1.5, 3, 4.5, 6, 6.7, 8.3, 9, 10.5, 12, 13.5, 14, and 14.5 cm. However, different main channel sinuosities (s) were constructed. Specifically, s = 1.37 (Shiono and Muto 1998) and 1.571 (Muto 1997). The velocity measurements were performed along half of a meander in the main channel at Dr = 0 (bankfull), 0.15 and 0.5. Thus, in the main channel, the means of the flow angles between the channel bed and bankfull and between the bankfull and water surface could be determined (see Figs. 4 and 5 in Shiono and Muto 1998 and Fig. 4.15 in Muto 1997). Then, the mean depth-averaged flow angle ($\theta_{a(m)}$) in the lateral direction was obtained.

(2) The experiments of Patra et al. (2012) were conducted in a 10-m-long and 0.52-m-wide compound channel with a valley slope (S) of 6.1‰. Quasi-uniform flow was achieved in the test reach for a given discharge by adjusting the tailgate at the downstream end of the flume. The

sinuosity of the main channel was 1.22. The width and depth of the main channel were both 10 cm, yielding b/h = 1. The lateral positions of the measurement lines in the main channel were $y \approx 0.5$, 2.8, 5, 7.3 and 9.5 cm. Detailed measurements were performed in two cases, with main channel flow depths (H) of 11.6 and 16.8 cm, yielding Dr = 0.14 and 0.4, respectively. However, in these cases, the mean depth-averaged flow angle ($\theta_{a(m)}$) was only available for apex sections (see Fig. 3 in Patra et al. 2012).

(3) The experiments of Shiono et al. (2009) were conducted in a 13-m-long and 2.4-m-wide flume with a valley slope (S) of 2‰. The water surface slope along the flume was controlled by tailgates at the flume end; thus, quasi-uniform flow was achieved by manually adjusting the tailgates. The geometrical angle, θ_{geo}, of the region between the entrance section and apex section was $60°$. The sinuosity of the main channel (s) was 1.384, and the main channel slope was 1.4‰. The width and depth of the main channel were 40 and 4 cm, respectively, resulting in b/h = 10. Uniform sand with a median sand diameter of d_{50} = 0.855 mm was placed in the meandering main channel. The sand depth was large enough to adequately cover the flume base during the experiments. Three pumps facilitated flow circulation. One pump was a sediment circulation pump that conveyed sediments back to the inlet of the flume through a recirculation pipe system. The bed morphology slightly changed after the experiments, yielding a Manning roughness coefficient that was nearly the same as that in the non-mobile case (estimated from Fig. 3 in Shiono et al. 2008). The smooth floodplain was made of Styrofoam. The velocity distribution was measured in detail at Dr = 0

(bankfull) and 0.3. The lateral interval of the measurement lines in the main channel was 2 cm, and the vertical interval between two vertical points was 5 mm. The measured mean depth-averaged flow angle ($\theta_{a(m)}$) along half of a meander was obtained from Figs. 4 and 5 in Shiono et al. (2009).

(4) Harrison et al. (2015) numerically simulated overbank flows (including magnitude and orientation) in a reach of the Merced River, California. This channel was reconstructed after a 50-year flood (the peak flow was 234 m^3/s), producing a single-threaded, meandering river. The geometrical angle, θ_{geo}, of the region between the entrance section and apex section was approximately $40°$ (estimated from Fig. 7 in Harrison et al. 2015). The width (b) and depth (h) of the main channel were 29 m and 1 m, respectively, yielding b/h = 29. The bend radius at the apex was ≈ 110 m. The floodplain width varied from 250 to 500 m, which was 9-17 times greater than the width of the main channel. The valley gradient (S) was 3‰, and the sinuosity of the main channel was 1.16; thus, the bed gradient of the main channel (S_{mc}) was 2.5‰. The reach had a gravel bed with d_{16} = 3.2 cm, d_{50} = 5.7 cm and d_{84} = 9.5 cm. A plan view of the meandering channel is shown in Fig. 1 of Harrison et al. (2015). The patterns of the depth-averaged velocity magnitude and orientation were simulated for a five-year flood. The floodplain flow depth was ≈ 0.5 m, and thus, $Dr \approx 0.3$. We performed predictions at the downstream bend because the floodplain gradient was stable (= 3‰) in the regions within 150 m on either side of the apex section in the bend. The θ_a values in the section with $\theta_x \approx 5°, 15°, 20°$ and $40°$ were extracted from

Fig. 7 in Harrison et al. (2015) to obtain modeled $\theta_{a(m)}$ values to validate the proposed model.

5 Results and Discussion

The predicted $\theta_{a(m)}$ is plotted against the measured $\theta_{a(m)}$ in Fig. 4. First, the predicted and measured values of $\theta_{a(m)}$ were compared in the non-mobile bed channels based on the data from our experiments and those of Shiono and Muto (1998), Muto (1997) and Patra (2012) (open points in Fig. 5). The comparison indicates that the predictions agree well with the measurements. Second, the measured $\theta_{a(m)}$ was compared to the predicted $\theta_{a(m)}$ in a meandering channel with a mobile bed. The experimental data were from Shiono et al. (2009) (solid triangles in Fig. 5). Although the bed morphology after the experiment was different from that before the experiment, the influence of the bedform on $\theta_{a(m)}$ can be neglected because the secondary current cell was fully developed and occupied the entire main channel in the apex sections (see Fig. 10 in Shiono et al. 2009). Fig. 5 shows that the predicted $\theta_{a(m)}$ is equal to the measured $\theta_{a(m)}$ within uncertainty. Third, good agreements between the predictions and measurements were obtained in the numerical simulation of a field study (crosses in Fig. 5). Overall, good agreements between the prediction and the laboratory observations and the numerical simulation demonstrate that the proposed model (Eq. (7)) can accurately predict the mean depth-averaged flow angle ($\theta_{a(m)}$) in a meandering main channel with overbank flows.

Because $\theta_{a(m)}$ can be predicted using *Dr* and *k* (see Eq. (7)), the variation between $\theta_{a(m)}$ and *Dr* can be observed, as shown in Fig. 6. k $(= \frac{\theta_x}{\theta_{geo}})$ is constant for a given section. Specifically, k = 1 at the entrance of a meander (e.g., CS5 in our study) because $\theta_x = \theta_{geo} = 60°$ and k = 0.5 in the middle section (e.g., CS6 in our study) because $\theta_x = 30°$. The data in Fig. 6 are from our study and those of Shiono and Muto (1998), Muto (1997) and Shiono et al. (2009), in which $\theta_{a(m)}$ was measured at the entrance section ($\theta_x = 60°$) and middle section ($\theta_x = 30°$). θ_{geo} is fixed for the region between the entrance section and apex section in a channel. The relation between $\theta_{a(m)}$ and *Dr* is linear in the entrance section (the blue line in Fig. 5) and the middle section (the red line). Dashed lines indicate 10% uncertainty in the predictions. The measured $\theta_{a(m)}$ values (points) are similar to the predictions (lines). For a given section (e.g., entrance section, $\theta_x = 60°$), a large *Dr* reflects the strong effects of upstream floodplain flow on the main channel flow, producing a high flow angle ($\theta_{a(m)}$), as visualized by Shiono and Muto (1998) (see Fig. 3 in their paper). However, the prediction in the entrance section (blue lines) is considerably greater than the prediction in the middle section (red lines), particularly under high-flow conditions (large *Dr*). This trend occurs because $\theta_{a(m)}$ is related to the square of θ_x (i.e., ${\theta_x}^2$) for a given *Dr* (see Eq. (7)). Thus, for a case with a fixed flow depth (*Dr*), a large flow angle ($\theta_{a(m)}$) will be observed in the entrance section because the section has a large θ_x.

Eqs. (6) and (7) indicate that the mean local flow angle above the secondary current cell, θ_{upper}, is one factor that influences the predicted

value of $\theta_{a(m)}$. Thus, the relation between the mean measured θ_{upper} ($\theta_{upper(m)}$) and *Dr* is discussed (Fig. 7). The discussion herein focuses on the measured $\theta_{upper(m)}$ for *Dr* = 0.15 to 0.5. The experimental data include the authors' own experiments (circles in Fig. 7) and those from Shiono and Muto (1998) (squares). Although $\theta_{upper(m)}$ is equal to θ_x at the meander entrance ($\theta_x = 60°$) within uncertainty, the value of $\theta_{upper(m)}$ decreases with decreasing *Dr* (black points) because the contribution of the upstream floodplain flow to the main channel flow above the secondary current cell decreases with the decrease of flow depth. In contrast, $\theta_{upper(m)}$ in the middle section (red points) is equal to θ_x ($= 30°$, red dashed line). Therefore, in a section with a large θ_x, the effect of upstream floodplain flow on θ_{upper} is reduced at the low flow depths (e.g., *Dr* < 0.15 in Fig. 7). Thus, the assumption that $\theta_{upper(m)} = \theta_x$ may lead to errors during the calculation, particularly for a section with a large θ_x under low-flow conditions (a small *Dr*). For example, at *Dr* = 0.15, the prediction of $\theta_{a(m)} = 9°$ using $\theta_x = 60°$, which is close to the predicted value of $\theta_{a(m)} = 7.4°$ using $\theta_{upper(m)} = 49.6°$. However, such a small difference (1.6°) is acceptable in practical applications.

Fig. 8 shows the lateral distribution of the measured θ_{upper} at different *Dr* to further discuss the variation of $\theta_{upper(m)}$ at low flow depths. The vertical wall at *y/b* = 1 connects the upstream floodplain. First, at the meander entrance ($\theta_x = 60°$, Fig. 8a), the water above the secondary current cell close to the upstream floodplain (close to *y/b* = 1) is significantly affected by upstream floodplain flow, producing a value

of θ_{upper} being equal to θ_x. This finding indicates that the water close to the upstream floodplain flows downstream in the valley direction. However, the water further from the upstream floodplain flows downstream close to the ridge direction, particularly at low flow depths (small *Dr*). At high flow depth (e.g. *Dr* = 0.5), $\theta_{upper(m)} = 60.4 \pm 1.3°$ (the black dashed line in Fig. 8a) means that the water above the cell in the entire main channel flows downstream in the valley direction. At a moderate flow depth (*Dr* = 0.35), $\theta_{upper} \approx 60°$ at *y/b* = 0.6 to 1 but decreases from $60°$ to $45°$ at *y/b* = 0.6 to 0. A more distinct decrease in θ_{upper} along *y/b* is observed under low-flow conditions (*Dr* = 0.15). Notably, θ_{upper} decreases continuously from $60°$ to $30°$ from *y/b* = 0.7 to 0, indicating that the influence of floodplain flow on the main channel flow above the secondary current cell is significantly reduced at the low flow depths. The main channel flow prefers to propagate downstream in the ridge direction at the low flow depths. Second, in the middle section with $\theta_x = 30°$, the flow above the cell moves downstream in the valley direction at *Dr* = 0.15 to 0.5, yielding $\theta_{upper(m)} = 31.2 \pm 2.7°$ (the gray line in Fig. 8b). Overall, the mean local flow angle above the secondary current cell (θ_{upper}) decreases far from the upstream floodplain under low-flow conditions at the entrance section ($\theta_x = 60°$, see Fig. 8a). Because of the small section angle ($\theta_x = 30°$) in the middle section, a distinct decrease in θ_{upper} may be observed at small flow depths (e.g., *Dr* = 0.05).

In the meandering main channel, $\theta_{a(m)}$ is related to the main channel discharge, Q_{mc} (Fig. 9). $\theta_{a(m)}$ is normalized by θ_{geo} ($= 60°$), and

Q_{mc} is normalized by the total discharge (Q). In cases with different values of Dr (= 0.25 to 0.45), the maximum and minimum values of Q_{mc}/Q occur in the apex section (points at $\theta_{a(m)}/\theta_{geo} \approx -0.05$ to 0 in Fig. 9) and entrance section (points at $\theta_{a(m)}/\theta_{geo} \approx 0.25$ to 0.5), respectively, indicating that the apex section has the greatest conveyance capability and the entrance section has the smallest conveyance capability. This result is consistent with previous observations (Shiono and Muto 1998; Liu et al. 2016a, b). Specifically, Liu et al. (2016a, b) reported that in the meandering main channel, the maximal mean velocity (discharge) occurred in apex sections (e.g., CS7) and the minimal mean velocity (discharge) occurred in crossover sections (e.g., CS5). In addition, the main channel discharge can be linked to secondary flow. The section with the greatest conveyance capability has the lowest intensity of secondary flows. At the apex, the secondary current cell is enhanced by centrifugal force, and the effect of floodplain flow can be ignored. In contrast, at entrance sections, secondary flow is enhanced by both the upstream floodplain flow and centrifugal force, yielding $\theta_{upper(m)} = \theta_x$, which effects the predictions of $\theta_{a(m)}$ and the main channel discharge. Ervine et al. (2000) proposed a secondary flow parameter to represent the intensity of the secondary flow and then combined this parameter and the lateral distribution method (LDM) to model the lateral distribution of the depth-averaged velocity in apex and crossover sections. Their result showed that the velocities in the apex sections were greater than those in the crossover sections. These findings are consistent with our measurements (see Fig. 9). Additionally, their modeling result demonstrated that the value of the secondary flow parameter (2%) in the apex

section was smaller than that (6%) in the crossover section, indicating that the intensities of secondary flow in apex sections is smaller than those in crossover sections. This result is consistent with the observations in our study (see Fig. 2). A numerical simulation further confirmed this phenomenon that the secondary flow in the entrance section is stronger than that in the apex section (Jing et al. 2009). Therefore, the stage-discharge relation (or the lateral distribution of the depth-averaged velocity) in the meandering channel is predicted in the apex section, as is done in certain models (e.g., Ervine et al. 2000; Huai et al. 2009; Shan et al. 2015, 2017; Liu et al. 2012, 2016a and b).

Finally, this model is proposed under quasi-uniform flow conditions. Further verification should be performed if the flow condition changes. The model can predict the flow angle between the entrance section and apex section in a meandering channel with b/h = 1 to 29 and s = 1.16 to 1.571 for Dr = 0 to 0.5. If the meandering main channel is extremely wide and shallow (i.e., b/h is extremely large), the development of a secondary current cell may be restricted, and thus, the model may not be able to accurately predict the depth-averaged flow angle. In addition, this model focuses on a smooth meandering channel with similar roughness parameters in the main channel and floodplain (i.e., $n_{mc} \approx n_{fp}$). However, vegetation is often present on floodplain beside the main channel. For example, lush grass is present on the floodplains of the Minjiang River in China (Fig. 1 in Yang et al. 2007) and on the floodplains of the River Blackwater in the UK (Figs. 2a and 3a in Gunawan et al. 2008). The proposed model cannot predict flow directions in a meandering channel with vegetation on the floodplains because this model does

not account for the resistance associated with vegetation. Dense vegetation leads to an increase in the overall Manning's roughness parameter n_{all} ($= \frac{A}{Q} R^{2/3} S^{1/2}$). The ratio of the roughness parameters is $n_{all(roughness)}/n_{all(smooth)} \geq 1.3$ (Liu et al. 2016a). When this ratio is satisfied, the flow pattern is similar in meandering compound channels with dense floodplain vegetation but different from the flow pattern in smooth channels. This trend occurs because vegetation may produce complex flow structures around stems and the canopy. For example, stem turbulence occurs behind an individual stem when $Re_d > 120$ (Liu and Nepf 2016), where Re_d ($= \frac{u_v d}{\nu}$) is the stem Reynolds number, where u_v is the velocity within a vegetated area and d is the stem diameter. Additionally, Kelvin-Helmholtz vortices will be formed at the canopy height when $ah_v > 0.1$, in which a (= md, where m is the vegetation density) is the frontal area per unit volume and h_v is the vegetation height (Nepf 2012). The increase in turbulence and decrease in velocity in the vegetated region leads to a change in the vertical profile of the local flow angle, producing a different depth-averaged flow angle ($\theta_{a(m)}$). Thus, the predictive model for such conditions must be further investigated.

6. Conclusions

This study proposed a model to estimate the lateral mean of the depth-averaged two-dimensional flow direction (i.e., the mean of the depth-averaged flow angle $\theta_{a(m)}$) between the entrance section and apex section in a meandering compound channel. Velocity measurements

are performed in a large-scale meandering compound channel. The value of $\theta_{a(m)}$ is highly related to the secondary current cell. The mean local flow angle above the secondary current cell, θ_{upper}, and the mean local flow angle within the cell, θ_{cell}, are discussed separately. Study shows that θ_{cell} is equal to 0°, and θ_{upper} is equal to the section angle, θ_x (Eq. (6)). Thus, $\theta_{a(m)}$ can be predicted using the geometrical angle, θ_{geo}, of the region the relative flow depth, *Dr*, and θ_x (Eq. (7)). The proposed model is validated using published experimental data from four laboratory experiments and a numerical simulation of one field study, covering a wide range of key flow parameters. Good agreement is obtained between the predictions and measurements, indicating that this model can accurately predict $\theta_{a(m)}$ in the region between the entrance section and apex section. The value of $\theta_{a(m)}$ is related to the conveyance capability of the meandering main channel. The apex section with $\theta_{a(m)} = 0°$ has the greatest conveyance capability. Finally, the limitations of the model are discussed. This model can be applied in a meandering channel with *b/h* = 1 to 29, *s* = 1.16 to 1.571, and *Dr* = 0 to 0.5.

Acknowledgments

This study was financially supported by the National Key Research and Development Program of China (No. 2016YFC0402302), the National Natural Science Foundation of China (Nos. 51609160 and 51539007), and the Open Fund from the State Key Laboratory of Hydraulics and

Mountain River Engineering, Sichuan University (SKHL1608). Constructive comments and suggestions made by the associate Editor and Reviewers have greatly improved the quality of the final manuscript.

Notation

A	=	cross-sectional area in an apex section;
a	=	frontal area per unit volume (= md);
B	=	channel width;
b	=	width of meandering main channel;
d_{16}, d_{50}, d_{84}	=	particle sizes;
Dr	=	relative flow depth (= (H-h)/H);
d	=	stem diameter;
H	=	flow depth in the meandering main channel;
h	=	bankfull level;
h_0	=	height of the secondary current cell;
$h_{0(c)}$	=	distance between the cell bottom (z = 0 cm) and center (z = $h_{0(c)}$);
h_v	=	vegetation height;

k	=	dimensionless coefficient ($= \frac{\theta_x}{\theta_{geo}}$);
L_w	=	wavelength in half of a meander (see Fig. 1);
L_v	=	valley length in half of a meander (see Fig. 1);
m	=	vegetation density;
N	=	the number of measurement lines (e.g., N = 13 in this study, see Fig. 1b);
n_{mc}, n_{fp}	=	Manning's roughness parameter in the main channel and floodplain, respectively;
n_{all}	=	overall Manning's roughness parameter;
Q	=	total discharge in the meandering compound channel;
Q_{mc}	=	main channel discharge;
R	=	hydraulic radius of the apex section;
Re	=	Reynolds number ($= \frac{QR}{Av}$);
Re_d	=	stem Reynolds number ($= \frac{u_v d}{\nu}$);
r	=	inner radius;
S	=	valley slope;
S_{mc}	=	slope of the meandering main channel;
s	=	sinuosity of the meandering main channel ($= L_w/L_v$);
U, V, W	=	time-averaged velocities in the streamwise, lateral and vertical directions, respectively;

u_v	=	velocity within a vegetated area;
x, y, z	=	streamwise, lateral and vertical coordinates, respectively (see Fig.1);
θ_a	=	depth-averaged two-dimensional flow direction ($= \frac{1}{H}\int_0^H \theta(z)\,dz$);
$\theta_{a(m)}$	=	lateral mean of θ_a ($= \sum_1^N \theta_a$);
θ_{cell}	=	local flow angle averaged over the height of the cell (see Eq.(3));
$\theta_{cell(m)}$	=	the mean value of θ_{cell} in the lateral direction ($= \frac{1}{b}\int_0^b \theta_{cell}\,dy$);
θ_{upper}	=	mean local flow angle above the cell (see Eq.(3));
$\theta_{upper(m)}$	=	mean value of θ_{upper} in the lateral direction ($= \frac{1}{b}\int_0^b \theta_{upper}\,dy$);
θ_{geo}	=	the geometrical angle of the region between the entrance section and apex section (see Fig.1);
θ_x	=	section angle (see Fig.1);
$\theta(z)$	=	local flow angle ($= arctan\frac{V}{U}$);
v	=	kinematic viscosity (= 10^{-6} m^2/s);

References

Blanckaert, K., 2010. Topographic steering, flow recirculation, velocity redistribution, and bed topography in sharp meander bends. Water Resources Research, 46, W09506. http://dx.doi.org/10.1029/2009WR008303

Chen, R., Shao, S., Liu, X., Zhou, X., 2015. Applications of Shallow Water SPH Model in Mountainous Rivers. Journal of Applied Fluid Mechanics, 8(4): 863-870. http://dx.doi.org/10.18869/acadpub.jafm.73.238.23311

Ding, Y., Liu, Y., Liu, X., Chen, R., Shao, S. 2017. Applications of Coupled Explicit–Implicit Solution of SWEs for Unsteady Flow in Yangtze River. Water, 9, 91. http://dx.doi.org/10.3390/w9030091

Ervine, D.A., Babaeyan-Koopaei, K., Sellin, R.H.J., 2000. Two-dimensional solution for straight and meandering overbank flows. Journal of Hydraulic Engineering, 126(9): 653-669. http://dx.doi.org/10.1061/(ASCE)0733-9429(2000)126:9(653)

Goring, D. G., Nikora, V. I. 2002. Despiking acoustic Doppler velocimeter data. Journal of Hydraulic Engineering, 128(1): 117-126. http://dx.doi.org/10.1061/(ASCE)0733-9429(2002)128:1(117)

Gunawan, B., Sun, X., Sterling, M., Knight, D.W., Shiono, K., Chandler, J.H., Rameshwaran, P., Wright, N.G., Sellin, R.H.J., Tang, X., Fujita, I., 2008. An integrated and novel approach to estimating the conveyance capacity of the River Blackwater, Proceedings of the Eight International Conference on Hydro-Science and Engineering, Nagoya, Japan, pp. 8-12.

Harrison, L.R., Dunne, T., Fisher, G.B., 2015. Hydraulic and geomorphic processes in an overbank flood along a meandering, gravel-bed river: implications for chute formation. Earth Surface Processes & Landforms, 40(9): 1239-1253. http://dx.doi.org/10.1002/esp.3717

Huai, W., Gao, M., Zeng, Y., Li, D., 2009. Two-dimensional analytical solution for compound channel flows with vegetated floodplains. Applied Mathematics and Mechanics, 30: 1121-1130. http://dx.doi.org/10.1007/s10483-009-0906-z

Jing, H., Guo, Y., Li, C., Zhang, J., 2009. Three-dimensional numerical simulation of compound meandering open channel flow by the Reynolds stress model. International journal for numerical methods in fluids, 59(8): 927-943. http://dx.doi.org/10.1002/fld.1855

Khatua, K.K., Patra, K.C., Mohanty, P.K., 2012. Stage-Discharge Prediction for Straight and Smooth Compound Channels with Wide Floodplains. Journal of Hydraulic Engineering, 138(1): 93-99. http://dx.doi.org/10.1061/(ASCE)HY.1943-7900.0000491

Liu, C., Nepf, H., 2016. Sediment deposition within and around a finite patch of model vegetation over a range of channel velocity. Water Resources Research 52, 600-612. http://dx.doi.org/10.1002/2015WR018249

Liu, C., Shan, Y., Liu, X., Yang, K., Liao, H., 2016a. The effect of floodplain grass on the flow characteristics of meandering compound channels. Journal of Hydrology, 542: 1-17. http://dx.doi.org/10.1016/j.jhydrol.2016.07.037

Liu, C., Shan, Y., Liu, X., Yang, K., 2016b. Method for assessing discharge in meandering compound channels, Proceedings of the Institution of Civil Engineers-Water Management, 169 (WM1): 17-29. http://dx.doi.org/10.1680/wama.14.00131

Liu, C., Wright, N., Liu, X., Yang, K., 2014. An analytical model for lateral depth-averaged velocity distributions along a meander in curved compound channels. Advances in Water Resources, 74: 26-43. http://dx.doi.org/10.1016/j.advwatres.2014.08.003

Liu, C., Luo, X., Liu, X., Yang, K., 2013. Modeling depth-averaged velocity and bed shear stress in compound channels with emergent and submerged vegetation. Advances in Water Resources 60, 148-159. http://dx.doi.org/10.1016/j.advwatres.2013.08.002

Liu, C., Yang, K., Liu, X., Huang, E., 2012. Analytical models for overbank flows in meandering channels with vegetated floodplains. Journal of Sichuan University (Engineering Science Edition), 44(6): 7-12. (in Chinese)

Lyness, J.F., Myers, W.R.C., Cassells, J.B.C., O'Sullivan, J.J., 2001. The influence of planform on flow resistance in mobile bed compound channels. Proceedings of the ICE-Water and Maritime Engineering, 148(1): 5-14. https://doi.org/10.1680/wame.2001.148.1.5

Muto, Yasunori, 1997. Turbulent flow in two-stage meandering channels. University of Bradford.

Nepf, H.M., 2012. Flow and transport in regions with aquatic vegetation. Annual Review of Fluid Mechanics 44, 123-142. http://dx.doi.org/10.1146/annurev-fluid-120710-101048

Sellin, R.H.J., Ervine, D.A., Willets, B.B., Ackers, P., 1993. Behaviour of meandering two-stage channels. Ice Proceedings Water Maritime & Energy, 112(2): 176-178. https://doi.org/10.1680/iwtme.1995.27663

Shan, Y., Liu, C., Luo, M., 2015. simple analytical model for depth-averaged velocity in meandering compound channels. Applied Mathematics and Mechanics, 36(6): 707–718. http://dx.doi.org/10.1007/s10483-015-1943-6

Shan, Y., Liu, X., Yang, K., Liu, C., 2017. Analytical model for stage-discharge estimation in meandering compound channels with submerged flexible vegetation. Advances in Water Resources, 2017, 108, 170-183. http://dx.doi.org/10.1016/j.advwatres.2017.07.021

Shiono, K., Chan, T.L., Spooner, J., Rameshwaran, P., Chandler, J.H., 2009. The effect of floodplain roughness on flow structures, bedforms and sediment transport rates in meandering channels with overbank flows: Part I. Journal of hydraulic research, 47(1): 5-19. http://dx.doi.org/10.3826/jhr.2009.2944-I

Shiono, K., Muto, Y., 1998. Complex flow mechanisms in compound meandering channels with overbank flow. J Fluid Mech, 376: 221-261. http://dx.doi.org/10.1017/S0022112098002869

Shiono, K., Spooner, J., Chan, T., Rameshwaran, P., Chandler, J., 2008. Flow characteristics in meandering channels with non-mobile. Journal of Hydraulic Research, 46(1): 113-132. http://dx.doi.org/10.1080/00221686.2008.9521848

Spooner, J., 2001. Flow structures in a compound meandering channel with flat and natural bedforms. Loughborough University.

Wormleaton, P.R., Sellin, R.H.J., Bryant, T., 2004. Flow structures in a two-stage channel with a mobile bed. Journal of Hydraulic Research, 42(2): 145-162. http://dx.doi.org/10.1080/00221686.2004.9628300

Yang, K., Cao, S., Knight, D.W., 2007. Flow patterns in compound channels with vegetated floodplains. Journal of Hydraulic Engineering, 133(2): 148-159. http://dx.doi.org/10.1061/(ASCE)0733-9429(2007)133:2(148)

Table 1. Experimental parameters in our study [a]

Case	Q (m^3/s)	H (cm)	Dr	h_0 (cm)			$h_{0(c)}$ (cm)			Q_{mc} (m^3/s)			Symbol
				CS5	CS6	CS7	CS5	CS6	CS7	CS5	CS6	CS7	
MV1	0.189	25.5	0.45	14.5±1.5	20.0±1.5	24.5±1.5	7.0±1.5	10.0±1.5	13.0±1.5	0.033	0.041	0.048	
MV2	0.113	21.6	0.35	13.0±1.5	16.0±1.5	20.5±1.5	7.0±1.5	8.5±1.5	11.5±1.5	0.024	0.030	0.034	○
MV3	0.085	18.9	0.26	14.5±1.5	16.0±1.5	17.5±1.5	7.0±1.5	8.5±1.5	10.0±1.5	0.023	0.026	0.029	

[a] Q is the total discharge; H is the flow depth in the main channel; Dr (= (H-h)/H) is the relative flow depth, in which h is the bankfull height; h_0 is the height of the secondary current cell; $h_{0(c)}$ (= h_0/2) is the distance between the cell bottom and center; and Q_{mc} is the main channel discharge. The details of the experimental setup were provided in Liu et al. (2014) and Shan et al. (2015).

Table 2. Experimental parameters in the published references [a]

Case	H (cm)	b (cm)	h (cm)	Dr	s	S (‰)	S_{mc} (‰)	r (m)	Symbol
SM-1 [b]	5.3	15	5.3	0	1.37	1	0.73	0.35	□
SM-2 [b]	6.24	15	5.3	0.15	1.37	1	0.73	0.35	
SM-3 [b]	10.6	15	5.3	0.5	1.37	1	0.73	0.35	
M-1 [c]	5.3	15	5.3	0	1.571	1	0.64	0.35	◇
M-2 [c]	6.24	15	5.3	0.15	1.571	1	0.64	0.35	
M-3 [c]	10.6	15	5.3	0.5	1.571	1	0.64	0.35	
P-1 [d]	11.63	10	10	0.14	1.22	6.1	5	unknown	☆
P-2 [d]	16.67	10	10	0.4	1.22	6.1	5	unknown	
S-1 [e]	4	40	4	0	1.384	2	1.45	0.565	Δ
S-2 [e]	5.71	40	4	0.3	1.384	2	1.45	0.565	
H-1 [f]	≈ 150	29	100	≈ 0.3	1.16	3	2.5	≈110	×

[a] b is the width of the main channel; s is the sinuosity of the main channel; S is the valley slope; S_{mc} (= S/s) is the main channel slope; and r is the radius of the test meander. The remaining notations have the same definitions as those in Table 1. In this paper, the symbols for each case are the same throughout the text and figures.
[b] The experimental data for SM-1 to SM-3 are from Shiono and Muto (1998).
[c] The experimental data for M-1 to M-3 are from Muto (2012).
[d] The experimental data for P-1 and P-2 are from Patra et al. (2004).
[e] The experimental data for S-1 and S-2 are from Shiono et al. (2009).
[f] The field observations and numerical simulation in H-1 are from Harrison et al. (2015).

Table 3. Summary of θ_{cell}, θ_{upper} and θ_{upper}/θ_x at the centerline of the secondary current cell in our study (MN1-MN3) [a]

Dr	θ_{cell} (°)			Mean ± SD (°)	θ_{upper} (°) and θ_{upper}/θ_x	
	CS5	CS6	CS7		CS5	CS6
0.45	1.3	1.1	-3.4	-0.3 ± 2.6	57.8 (1.0) [b]	34.1 (1.1) [b]
0.35	-1.6	2.4	-1.5	-0.3 ± 2.3	60.1 (1.0) [b]	36.0 (1.2) [b]
0.25	2.1	1.6	-2.9	0.3 ± 2.7	61.9 (1.0) [b]	38.5 (1.3) [b]

[a] θ_{cell} ($=\frac{1}{h_0}\int_0^{h_0}\theta\,(z)dz$) is the mean of the local flow angles within the secondary current cell; θ_{upper} ($=\frac{1}{H-h_0}\int_{h_0}^{H}\theta\,(z)dz$) is the mean of the local flow angle above the secondary current cell; "Mean" indicates the mean of θ_{cell}; and "SD" indicates the standard deviation of θ_{cell}.
[b] The numbers in parentheses are the values of θ_{upper}/θ_x with a section angle $\theta_x = 60°$ at CS5

and $\theta_x = 30°$ at CS6.

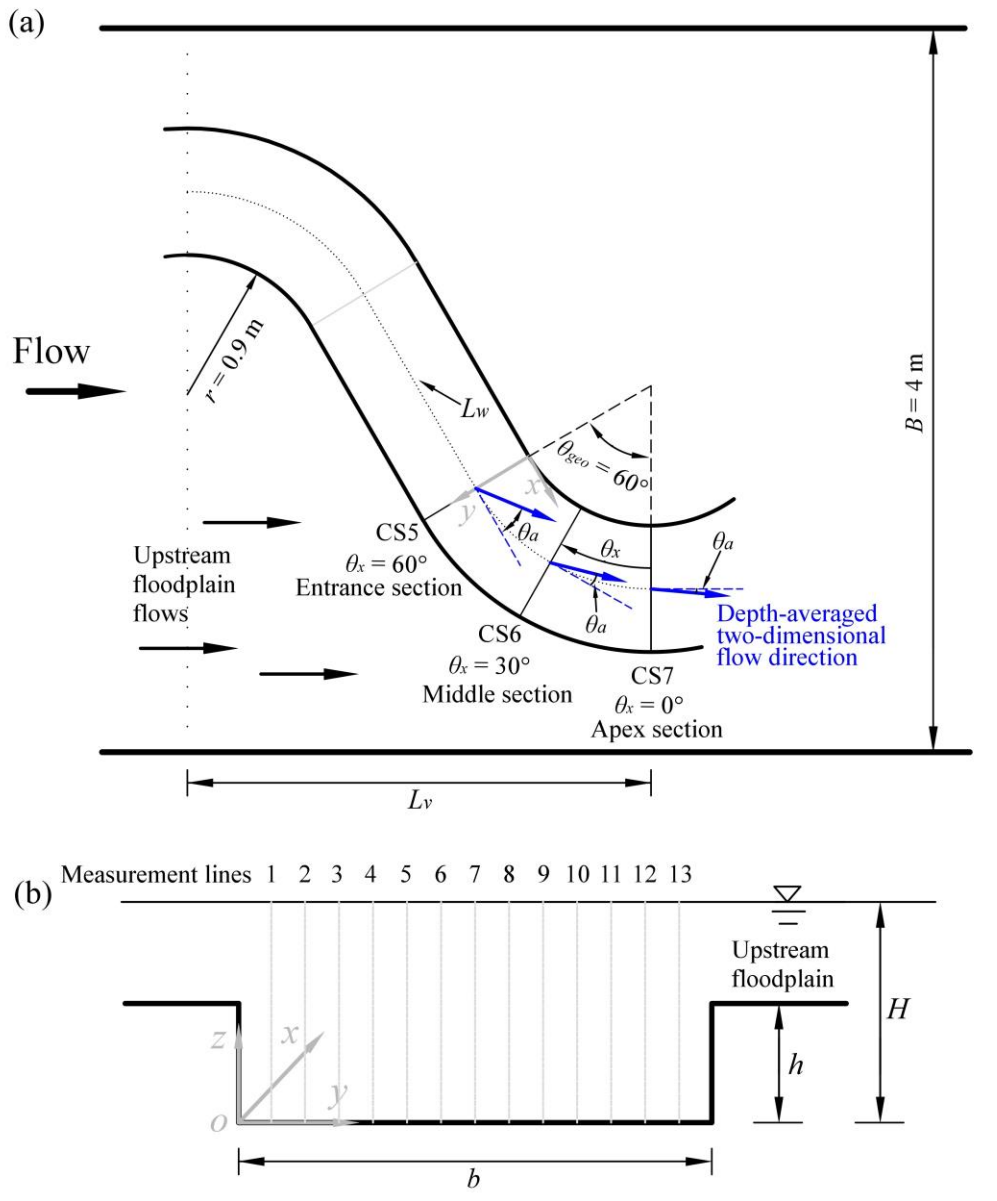

Fig. 1 Plan view of the channel geometry of the meandering compound channel; (b) Geometrical size of the meandering main channel. The sinuosity ($s = L_w/L_v$) is the ratio of the wavelength (L_w) to the valley length (L_v) in half a meander. CS5, CS6, and CS7 are the entrance section, middle section and apex section, respectively. The depth-averaged two-dimensional flow direction (depth-averaged flow angle) is predicted in the region between the entrance section and apex section. θ_{geo} is the geometrical angle of the region between the entrance section and apex section. θ_x is the section angle, indicating the angle from apex section to target section; e.g., $\theta_x = 30°$ at CS6. θ_a is the depth-averaged flow angle. H and h are the flow depth and bankfull depth, respectively. B (= 4 m) is the channel width, and b (= 0.7 m) is the main channel width. The measurement lines are numbered 1 to 13.

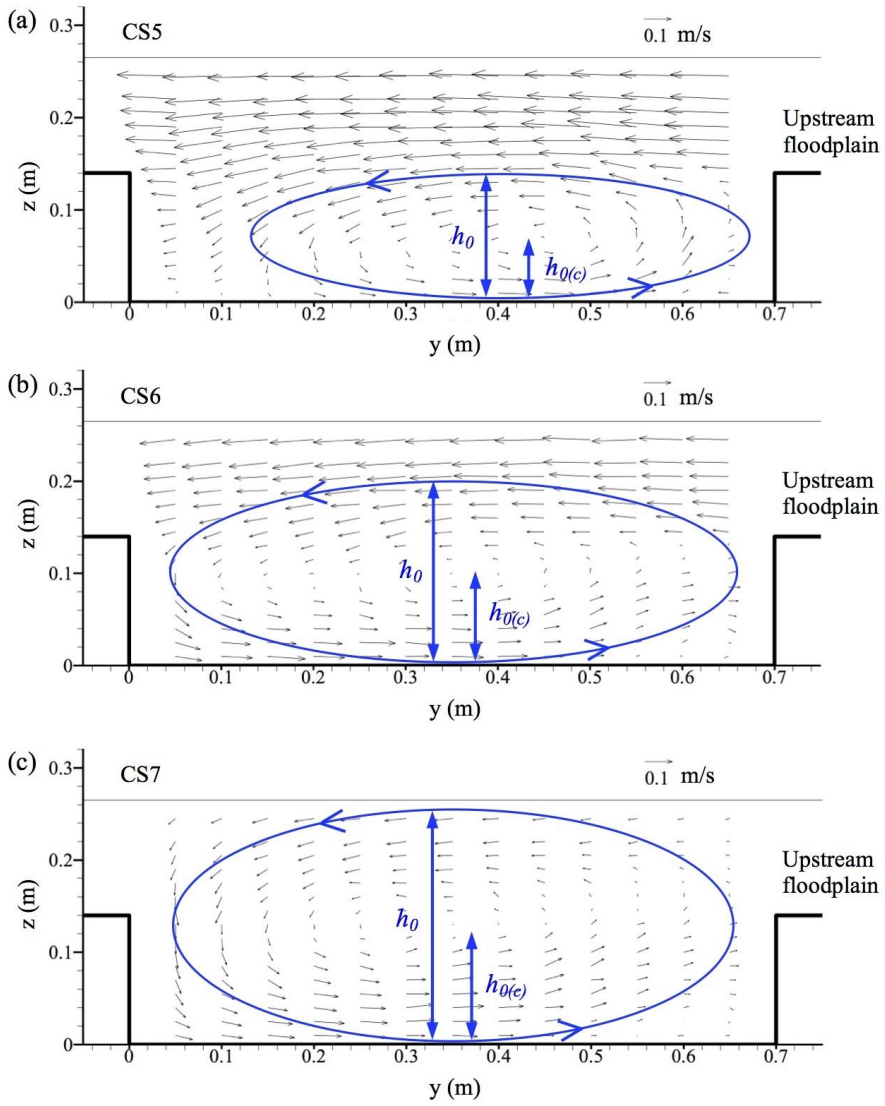

Fig. 2. Secondary current cell at (a) the meander entrance, CS5; (b) the middle section, CS6; and (c) the apex section, CS7 based on the measurements from case MN1. Relative flow depth Dr = 0.45 in MN1. z = 0 indicates the channel bed. The vertical wall at y = 0.7 m connected the upstream floodplain. A blue circle with arrows indicates the secondary current cell in the three sections. h_0 is the height of the cell. $h_{0(c)}$ (= h_0/2) is the distance between the bottom of the cell and the center of the cell.

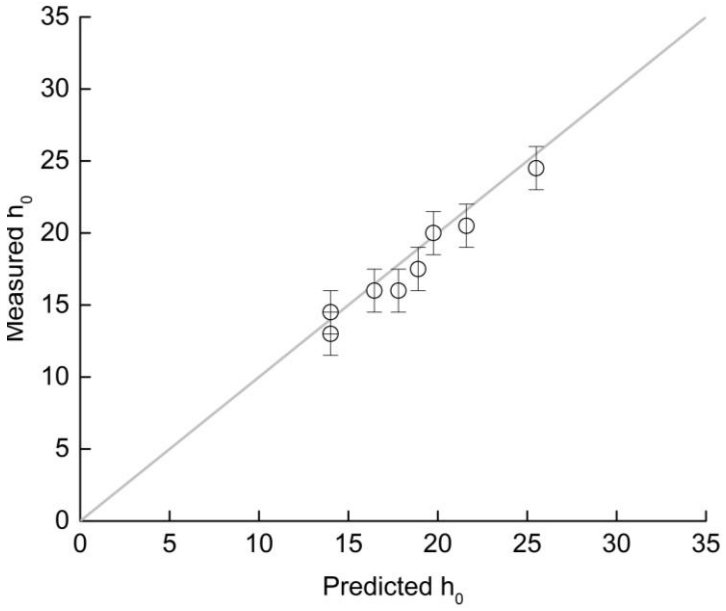

Fig. 3 Comparison of the measured and predicted h_0, based on our experimental data. The prediction is calculated by $h_0 = H - k(H - h)$, where $k = \frac{\theta_x}{\theta_{geo}}$.

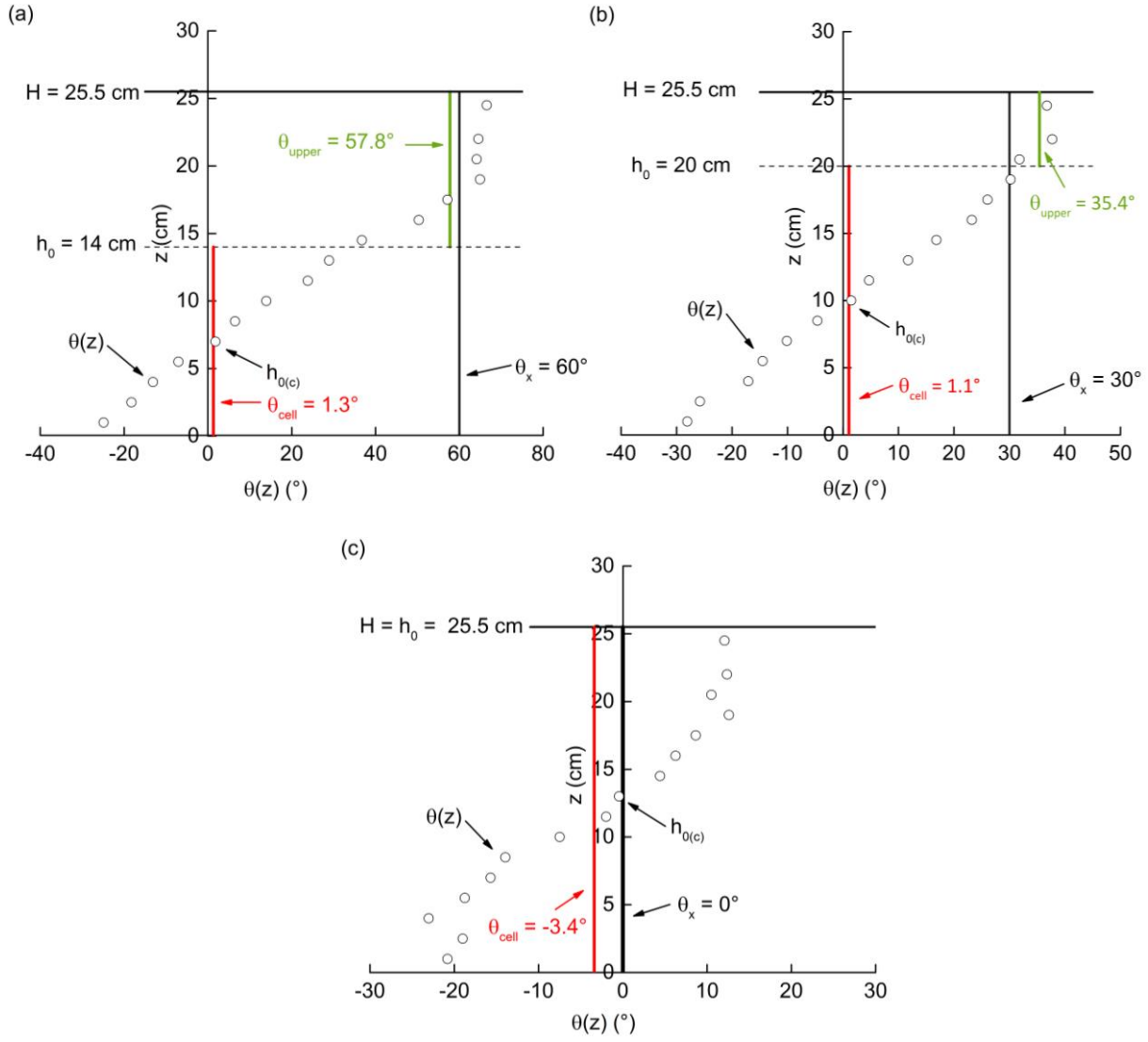

Fig. 4. Vertical distribution of the local flow angle, $\theta(z)$, at the centerline of the secondary current cell in the main channel in (a) CS5, (b) CS6 and (c) CS7 based on the experimental data from MN1 (see parameters in Table 1). H is the flow depth; h_0 is the height of secondary current cell; θ_{cell} $(= \frac{1}{h_0}\int_0^{h_0} \theta\,(z)dz)$ is the mean of the local flow angles within the secondary current cell; θ_{upper} $(= \frac{1}{H-h_0}\int_{h_0}^{H} \theta\,(z)dz)$ is the mean of the local flow angles above the secondary current cell; and $h_{0(c)}$ $(= h_0/2)$ is the distance between the cell bottom and center.

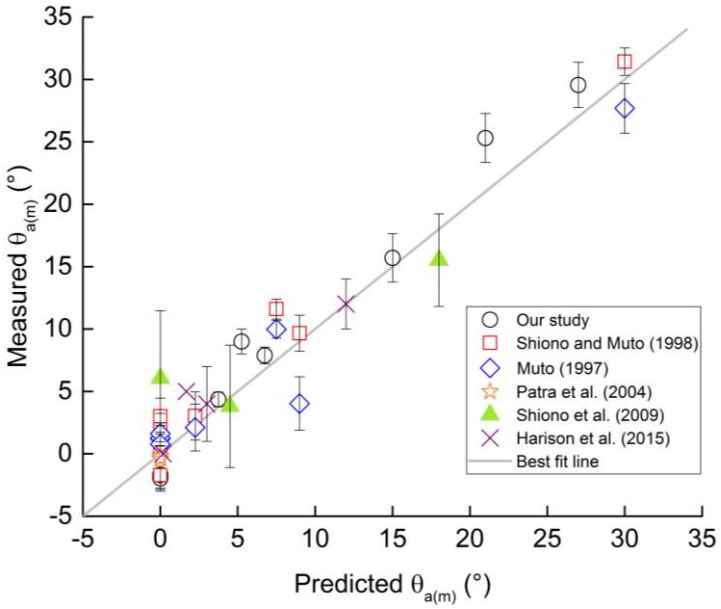

Fig. 5. Comparison of the measured and predicted $\theta_{a(m)}$ based on the data from our experiments and five published references.

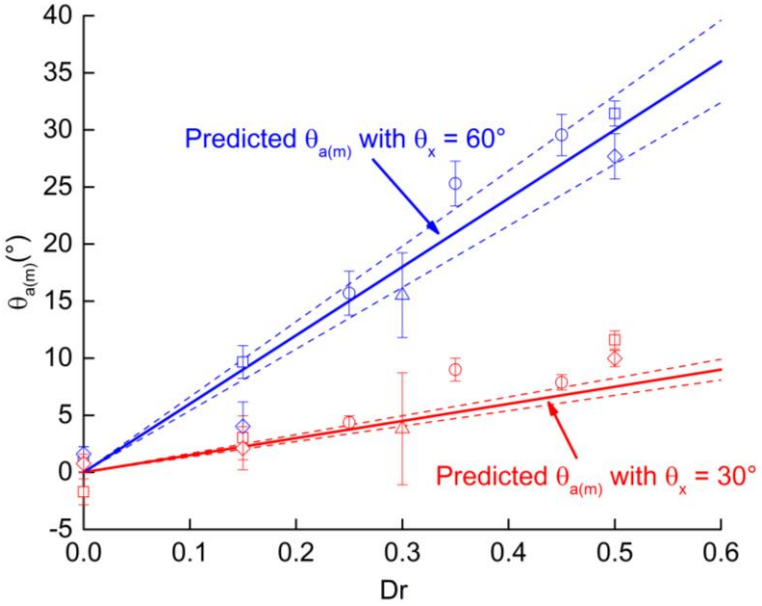

Fig. 6. Relation between $\theta_{a(m)}$ and Dr at the meander entrance (θ_x = 60°, blue points and lines) and middle section (θ_x = 30°, red points and lines). The dashed lines indicate the 10% uncertainty of the predictions. Experimental data are from our study and those of Shiono and Muto (1998), Muto (1997) and Shiono et al. (2009).

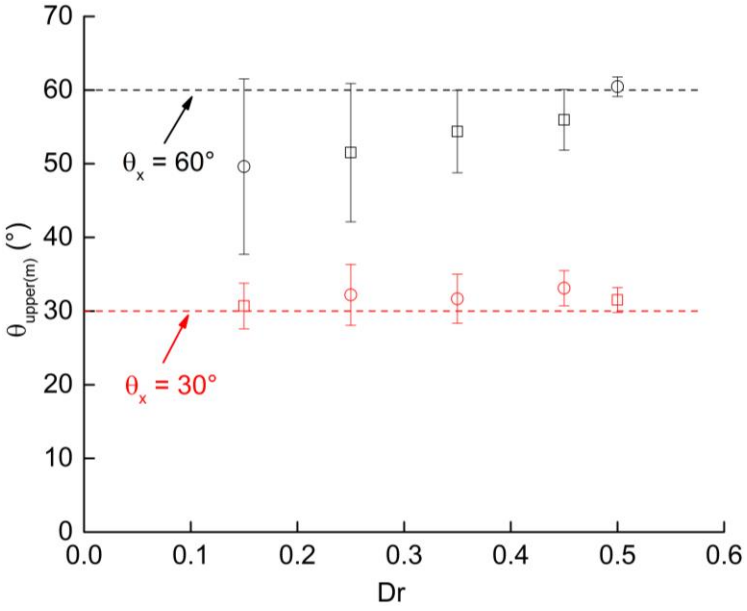

Fig. 7. Mean of the local flow angles above the secondary current cell, $\theta_{upper(m)}$, versus *Dr* in the entrance section (black points) and middle section (red points). The black and red dashed lines represent $\theta_x = 60°$ in the entrance section and $\theta_x = 30°$ in the middle section, respectively. Experimental data are from our study and that of Shiono and Muto (1998).

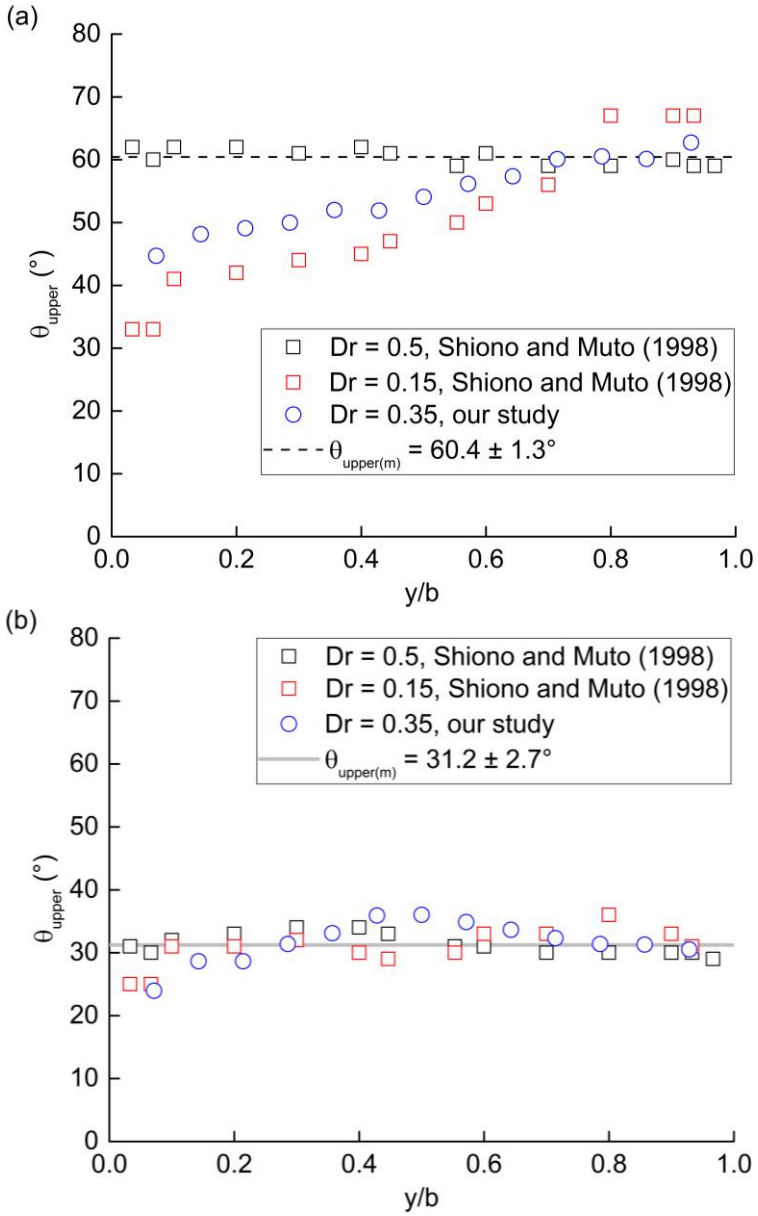

Fig. 8. The mean of the local flow angles above the secondary current cell, θ_{upper}, versus the normalized lateral distance, *y/b*, at different *Dr* at (a) the entrance section with $\theta_x = 60°$ and (b) the middle section with $\theta_x = 30°$. *b* is the width of main channel. The vertical wall at *y/b* = 1 connected the upstream floodplain. $\theta_{upper(m)} = 60.4 \pm 1.3°$ (the black dashed line in (a)) for the case of *Dr* = 0.5 from Shiono and Muto (1998). $\theta_{upper(m)} = 31.2 \pm 2.7°$ (the gray solid line in (b)) for the three cases of *Dr* = 0.5, 0.35 and 0.15 from Shiono and Muto (1998) and our study.

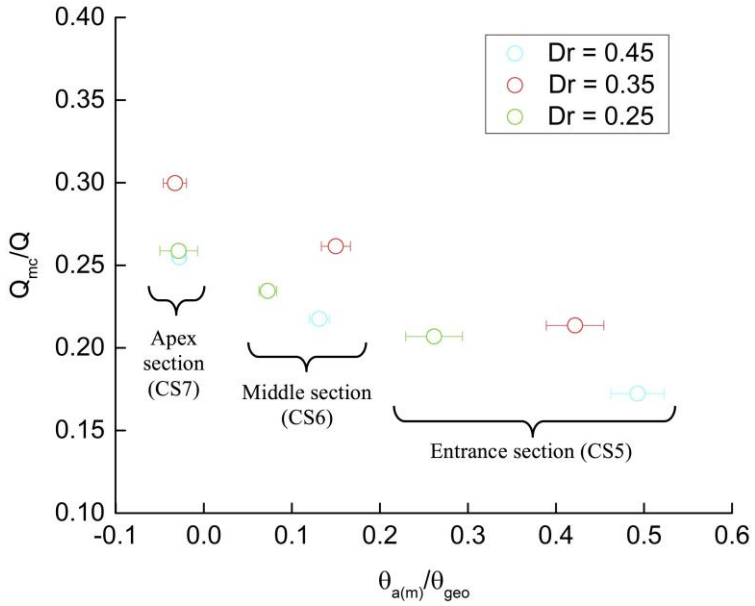

Fig. 9. Normalized main channel discharge, Q_{mc}/Q, versus the normalized mean of depth-averaged flow angles, $\theta_{a(m)}/\theta_{geo}$, in the apex section (CS7), middle section (CS6) and entrance section (CS5), where Q is the total discharge and $\theta_{geo} = 60°$. Experimental data are from our study.